Chinese Chemical Letters 37 (2026) 112065

Contents lists available at ScienceDirect

Chinese Chemical Letters

journal homepage: www.elsevier.com/locate/cclet

Mimicking tollgate-highway systems by cellulose-MXene networks in MMMs for enhancing CO_2 separation

Yong Zhang[1], Jiangnan Yu[1], Chao Liang, Zhaomin Li*, Xueqin Li*

School of Chemistry and Chemical Engineering/State Key Laboratory Incubation Base for Green Processing of Chemical Engineering, Shihezi University, Shihezi 832003, China

ARTICLE INFO

Article history:
Received 15 April 2025
Revised 8 September 2025
Accepted 5 November 2025
Available online 5 November 2025

Keywords:
Mixed matrix membrane
Tollgate-highway
MXene
Hydrogen bond
CO_2 separation

ABSTRACT

In gas separation mixed matrix membranes (MMMs), the interlayer stacking of nanosheet fillers directly leads to tortuous transport pathways that significantly reduce both membrane permeability and selectivity. To solve this issue, this study employs cellulose (MC) to interweave MXene for preparing cellulose-MXene (MC-MX) networks, which are then mixed with Pebax MH 1657 to prepare MMMs for enhancing CO_2 separation performance. The MC-MX network mimics the tollgate-highway system within the MMMs. In this system, MX acts as a selective tollgate that preferentially recognizes CO_2 through hydrogen bond interactions while improving CO_2/CH_4 selectivity in MMMs. Meanwhile, the hydroxyl–rich surfaces of MC provide low-resistance transport highway for accelerated CO_2 transport within the MMMs. Compared to the pure Pebax membrane, the CO_2 permeability of the Pebax/MC-MX-1wt% MMM increases to 580.46 Barrer (97 %), and the CO_2/CH_4 selectivity increased to 41.48 (70 %). Furthermore, the separation performance of the Pebax/MC-MX-1wt% MMM approaches the 2019 upper bound. The research results indicate that the tollgate-highway strategy effectively improves CO_2/CH_4 separation performance in MMMs, offering practical implications for the rational design of high-performance membranes.

© 2026 Published by Elsevier B.V. on behalf of Chinese Chemical Society and Institute of Materia Medica, Chinese Academy of Medical Sciences.

The utilization of biogas as an energy source has garnered significant research interest, but the presence of CO_2 reduces its calorific value [1,2]. Traditional separation methods (such as absorption and cryogenic separation) are usually energy-intensive [3,4]. Membrane separation are recognized as viable options owing to their operational simplicity, environmental sustainability and high energy efficiency [5]. The development of polymer membranes is constrained by the inherent trade-off between permeability and selectivity [6]. Current research on membrane-based CO_2 separation primarily focuses on addressing the permeability-selectivity trade-off in polymer membranes by developing advanced fillers for mixed matrix membranes (MMMs) [7,8]. It is key to explore new fillers to overcome the trade-off effect within the MMMs.

Two-dimensional (2D) materials have attracted significant research attention in gas separation [9]. As an emerging 2D material, MXene shows a significant potential as a filler for MMMs [10]. Liu *et al.* reported that Pebax/MXene MMMs with 0.5 wt% MXene loading achieved a CO_2/N_2 selectivity of 72.5 and CO_2 permeability of 21.6 GPU [11]. The incorporation of MXene significantly enhances CO_2 selectivity of in MMMs, while the improvement on CO_2 permeability remains constrained by interlayer stacking of MXene. Guan *et al.* fabricated Pebax/m-MXene MMMs with 0.5 wt% MXene loading for CO_2/N_2 separation, achieving a CO_2 permeability of 104.8 Barrer and selectivity of 82.2 [12]. The 2D MXene structure creates tortuous gas transport pathways, which increases CO_2/N_2 selectivity while compromising enhancement on CO_2 permeability [13].

The above literatures show that the 2D structure and surface -OH sites of MXene can effectively enhance the CO_2 separation selectivity of MMMs. However, the interlayer stacking of MXene results in the two negative outcomes: On one hand, the physical barrier formed by interlayer stacking significantly increases the tortuosity of the gas transport pathways, thereby decreasing CO_2 permeability [14]. On the other hand, the interlayer stacking reduces the exposure of -OH sites, and its limits the selective recognition for CO_2 [15,16]. Therefore, the interlayer stacking of MXene limits the simultaneous enhancement on CO_2 permeability and selectivity of MMMs.

To overcome the interlayer stacking of MXene, we designed a cellulose interwoven MXene composite filler (MC-MX) to enhance simultaneously CO_2 permeability and selectivity of MMMs

* Corresponding authors.
E-mail addresses: lizhm@upc.edu.cn (Z. Li), lixueqin861003@163.com (X. Li).
[1] These authors contributed equally to this work.

https://doi.org/10.1016/j.cclet.2025.112065
1001-8417/© 2026 Published by Elsevier B.V. on behalf of Chinese Chemical Society and Institute of Materia Medica, Chinese Academy of Medical Sciences.

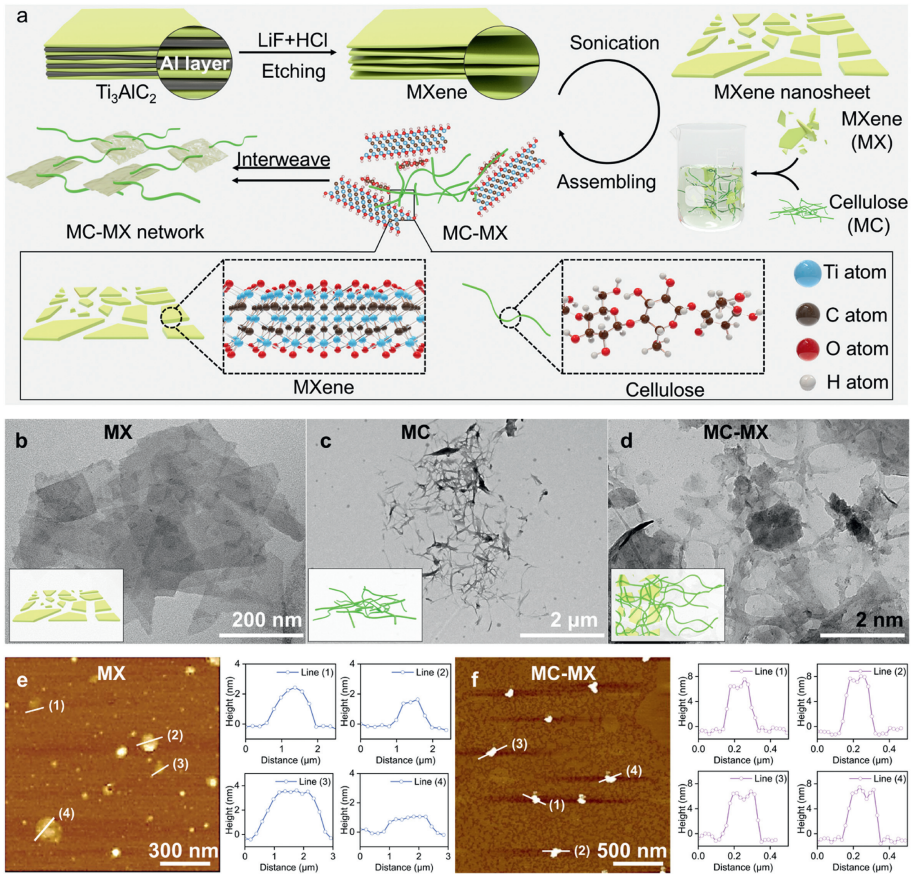


Fig. 1. (a) Schematic diagram of the preparation of MC-MX. (b) TEM image of MX. (c) TEM image of MC. (d) TEM image of MC-MX. (e) AFM of MX nanosheets. (f) AFM of MC-MX. Inset shows the thickness distribution of the MX nanosheets on the delineated line.

[17,18]. 1D MC physically suppresses interlayer stacking by interweaving MX to construct the continuous gas transport channels for forming CO_2 "highways" within the MMM. This structure significantly reduces CO_2 diffusion resistance and simultaneously enhances permeability. The -OH sites enriched on the MX surface form a "tollgate" through hydrogen bonding interactions, which preferentially recognize CO_2 to enhance selectivity. The structural design of MC-MX can enhance simultaneously both CO_2 permeability and selectivity of MMMs. This strategy overcomes the limitation on CO_2 separation performance of traditional MX-based MMMs.

In this paper, we prepared MC-MX networks by MC interwoven with MX. The MC-MX were mixed within a Pebax matrix to construct Pebax/MC-MX MMMs with enhanced CO_2/CH_4 separation performance. The structure, morphology and composition characteristics of MC-MX were extensively studied by characterization techniques. Subsequently, the CO_2 separation performance of Pebax/MC-MX MMMs is evaluated through CO_2/CH_4 permeation tests. The transport mechanism of CO_2 in Pebax/MC-MX MMMs was revealed by density functional theory (DFT).

Inspired by the tollgate-highway system, a physical blending strategy was used to synthesize MC-MX composite materials (Fig. 1a). This was driven by hydrogen bond interactions between the OH groups on their surfaces. Transmission electron microscopy (TEM) revealed a flat and almost transparent lamellar morphology of MX with an average lateral size of several hundred nanometers (Fig. 1b). The TEM images showed that the MC sample exhibited a three-dimensional interconnected network of nanofibers, and the MC modified MC-MX composite material exhibited a porous network structures (Figs. 1c and d). Furthermore, the atomic force microscopy (AFM) image of MC-MX material showed an increased thickness, indicating the successful intertwining of MX with MC (Figs. 1e and f). The network structure of MC-MX composite facilitated the effective permeation of CO_2 in MMMs.

The crystal structures of MC, MX, and MC-MX were evaluated using X-ray diffraction (XRD) analysis, as shown in Fig. 2a. Compared with MX, the diffraction peaks of 22.38° and 34.57° in MC-MX were consistent with those of MC, indicating successful introduction of MC. It is worth noting that the (002) peak of MC-MX shifted towards lower angles, indicating that MC further expanded the interlayer space of MX [19].

As shown in Fig. 2b, the Fourier transform infrared spectroscopy (FT-IR) spectrum of MX showed two prominent broad bands at 3446 and 532 cm^{-1}, which indicated the stretching vibrations of -OH and Ti-OH groups, respectively [20]. MC exhibits a characteristic absorption band associated with the stretching vibration of -OH at 3427 cm^{-1} [21]. The MC-MX sample had a peak at around 1060 cm^{-1} that corresponded to the C-O-C group of MC indicating that MC had been incorporated into MC-MX [22]. Additionally, a broadened band appearing between 3300 and 3500 cm^{-1} was indicative of stretching vibrations from OH group, thereby confirming the incorporation of MC into MX. Furthermore, the FT-IR spectrum of the MC-MX composite material demonstrated a blue shift ranging from 3427 cm^{-1} to 3446 cm^{-1}, which signified an enhanced hydrogen bonding interaction between MC and MX [23].

The thermal stability of the MC-MX composite material was investigated by thermogravimetric analysis (TGA) under an N_2 atmosphere (Fig. 2c and Fig. S4 in Supporting information). The MC-MX underwent a weight loss of 58.29% between 200 °C and 350 °C (Table S1 in Supporting information). The loss observed was attributed to the effective loading of MC, confirming the successful incorporation of MC into the MC-MX.

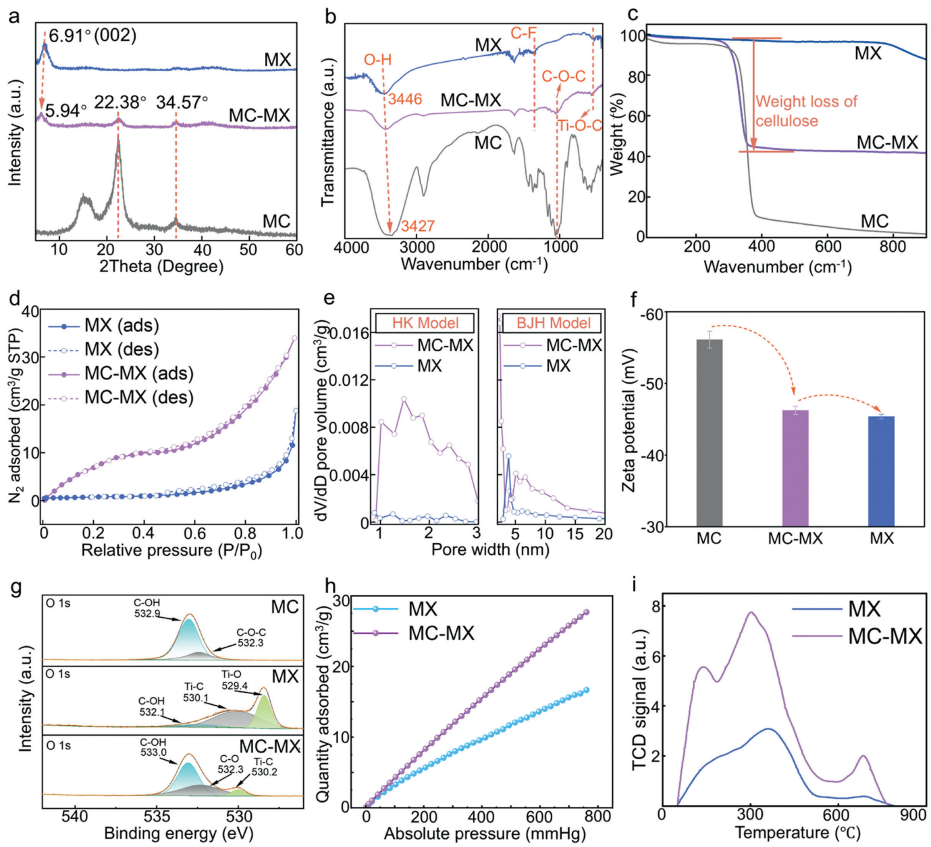


Fig. 2. (a) XRD patterns and (b) FT-IR spectra of MX, MC and MC-MX. (c) TG curves. (d) N_2 adsorption-desorption isotherm. (e) Pore size distribution. (f) Zeta potential of MC, MX and MC-MX samples at pH 7. (g) The high-resolution O 1s XPS spectra. (h) CO_2 adsorption isotherms at 298 K for MX and MC-MX. (i) CO_2 TPD profiles of CO_2 desorption.

To evaluate the porosity characteristics of MC-MX, N_2 adsorption−desorption was measured at 77 K (Figs. 2d and e, Fig. S5 and Table S2 in Supporting information). The specific surface area of the MC was 337.29 m^2/g. The specific surface area of MC-MX increased to 38.07 m^2/g, a significant rise from the 2.72 m^2/g of MX. This increase indicated that MC effectively constructed a network structure within the MC-MX, enhancing the MC-MX specific surface area. The pore size distribution of MC-MX (Fig. 2e) exhibits a broadened range compared to MX. Although the pore sizes of MC-MX were significantly larger than the kinetic diameters of both CO_2 and CH_4, the hierarchical pore architecture effectively optimized gas transport pathways, leading to a notable enhancement in the separation performance of the MMMs.

Further investigation was conducted into the change in zeta potential at pH 7, as shown in Fig. 2f and Table S3 (Supporting information). At pH 7, the zeta potential of MC exhibited pronounced negative charge (−65.22 mV), while the MX sample also carried a negative charge (−54.75 mV) due to the presence of surface hydroxyl groups. Following the formation of the MC-MX composite, there was an enhancement in the negative charge, with the zeta potential reaching a more negative value (−58.33 eV), indicating the successful self-assembly and attachment of MC onto the MX surface.

The X-ray photoelectron spectroscopy (XPS) spectrum of MX showed that there were peaks corresponding to F 1s, O 1s, Ti 2p, and C 1s at binding energies of 685.5, 529.7, 455.4, and 284.8 eV, respectively (Fig. 2g and Fig. S6 in Supporting information). When combined with MC, the C 1s and O 1s peaks in the MC-MX sample became stronger, while the Ti peak weakened (Fig. 2g). Furthermore, MC-MX exhibited characteristic C–O fitting peaks in the C 1s and O 1s spectroscopic regions through fitting analysis, indicating that the OH functional group was successfully introduced by MC (Fig. S6) [24].

Fig. 2h showed the CO_2 adsorption isotherm of MX and MC-MX at 25 °C. It was observed that the introduction of MC in MX-MX greatly improved the CO_2 adsorption capacity, indicating that the MC was effective in improving the CO_2 affinity capacity of MC-MX. The CO_2 adsorption capacity at 25 °C and 1 bar could be ordered in the follow: MX-MC > MX.

The CO_2 adsorption affinity of MX and MC-MX was investigated by temperature-programmed desorption (CO_2-TPD). As shown in Fig. 2i and Table S4 (Supporting information), MC-MX exhibited a prominent TCD signal peak at 300 °C, accompanied by intense CO_2 signals in mass spectrometry, indicating stronger CO_2 adsorption capacity compared to MX. The presence of a desorption peak at 100 °C in the CO_2-TPD of MC-MX could be attributed to affinity sites (-OH groups) introduced by MC, which not only confirmed the successful incorporation of the MC network but also aligns with the reported role of hydroxyl groups in CO_2 adsorption [25]. Furthermore, the enhanced specific surface area and porosity of MC-MX synergistically promoted CO_2 transport throughout the MC-MX. These results collectively demonstrate that the interwoven MC network in MC-MX serves as both a structural spacer and CO_2 affinity regulator.

The pure Pebax membrane and MMMs were characterized using cross- sectional images. As shown in Fig. S8 (Supporting information), MC-MX exhibited uniform distribution in the Pebax matrix at 0.5–1.5 wt% loading, confirming good compatibility between the components. When the loading of MC-MX composite material was increased to 2.0 wt%, although there was a certain degree of enrichment at the bottom, no significant defects were observed. The uniform distribution of MC-MX in the Pebax could

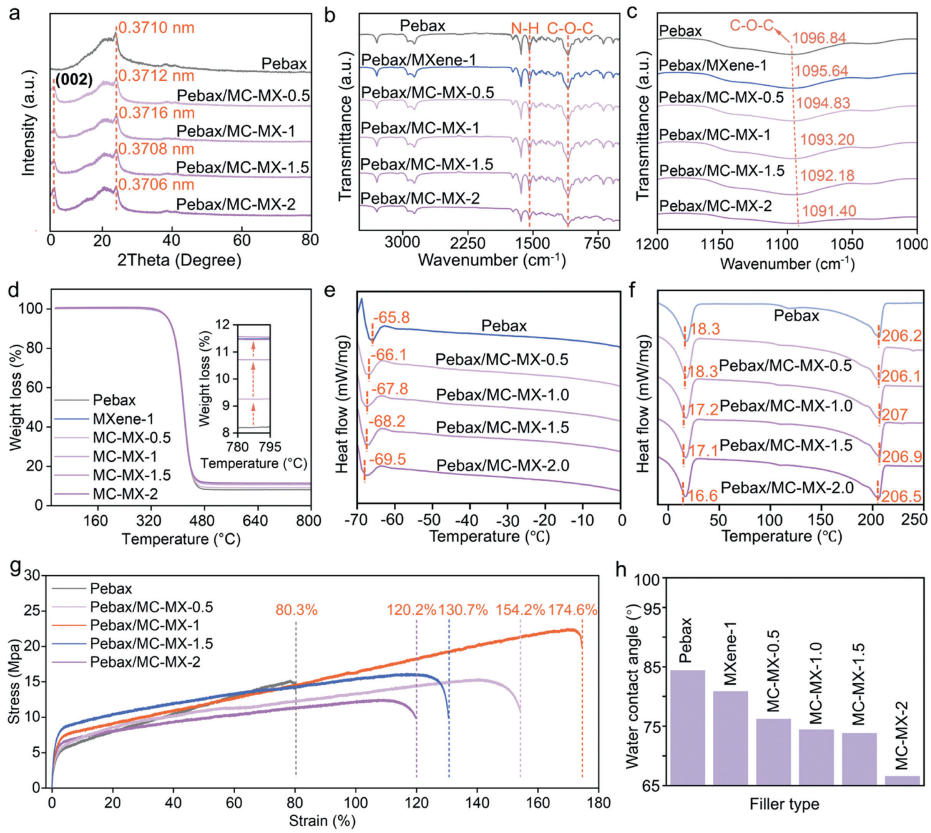


Fig. 3. (a) XRD spectra. (b, c) FT-IR curves. (d) TGA curves of MMMs. (e) T_g curves. (f) The melting peak temperature. (g) Tensile stress-strain curve and (h) the water contact angle of the Pebax membranes and Pebax/MC-MX MMMs.

be attributed to hydrogen bonding interactions formed between the hydroxyl groups of MC-MX and the ether/amide moieties of the Pebax polymer chains, which effectively suppressed filler agglomeration and mitigated defect formation. The energy dispersive spectroscopy (EDS) of Pebax/MC-MX membrane cross-section was measured, which showed that MC-MX was homogenously distributed within the membrane (Fig. S7 in Supporting information).

The crystalline properties of Pebax and Pebax/MC-MX films were characterized by XRD. As shown in Fig. 3a, Pebax had a typical amorphous structure, so the Pebax film showed a broad diffraction peak at 20°–24° [26]. The X-ray diffraction peaks of Pebax/MC-MX MMMs gradually increased with the increase of MC-MX loading, demonstrating that the structural stability of MC-MX was maintained during the film preparation process.

As shown in Figs. 3b and c, the characteristic spectral bands at 1560 cm^{-1} and 1096 cm^{-1} corresponded to the N–H bond and aromatic C–O-C bond stretching vibrations of Pebax [27,28]. The position of the C–O-C bond showed a significant red shift compared with the pure Pebax membrane, indicating a clear hydrogen bond interaction between MC-MX and Pebax [29]. As shown in Fig. 3d and Table S5 (Supporting information), the residual mass of the Pebax/MC-MX MMMs increased with the increase of the MC-MX loading, indicating that MC-MX had been successfully loaded. The MMMs demonstrated thermal stability, which is attributed to strong hydrogen bonding between the polymer and MC-MX, mitigating interfacial debonding induced by thermal expansion mismatch.

Differential scanning calorimetry (DSC) profiles in Figs. 3e and f revealed two critical thermal parameters: The glass transition temperature (T_g) and the melting temperature (T_m). The pure Pebax polymer exhibited two endothermic peaks at 18.3 °C (PEO soft segments) and 206.2 °C (PA rigid domains), characteristic of its multi-block copolymer architecture [30]. The incorporation of MC-MX reduced the T_g of Pebax through hydrogen bonding and enhanced the chain mobility. The improvement of the Pebax chain mobility was conducive to enhancing the permeability of MMMs. As shown in Table S6 (Supporting information), the decrease in crystallinity

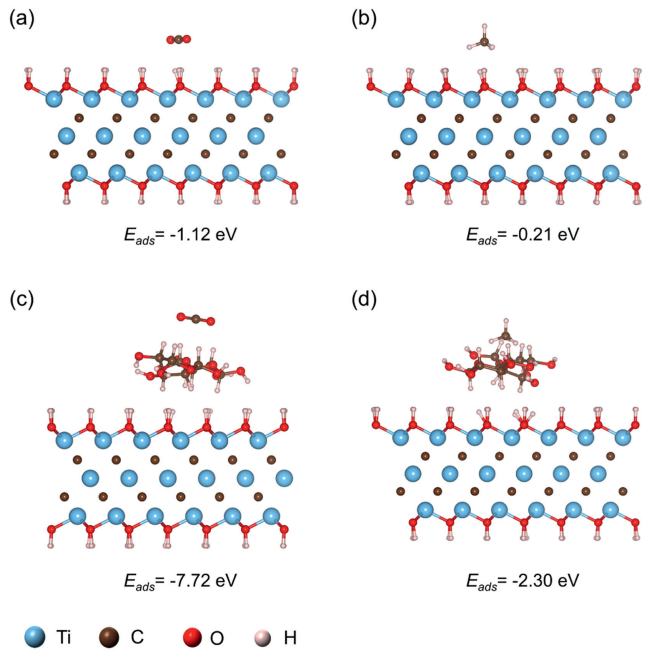


Fig. 4. The optimized binding sites and binding energies of CO_2 and CH_4 within (a, b) MX, and (c, d) MC-MX.

enhanced the chain mobility of Pebax, thereby increasing the permeability of CO_2 within the MMMs.

As depicted in Fig. 3g, the Young's modulus of the Pebax membrane was 843.9 MPa, with an elongation at break of 13.22 % and a tensile strength at break of 37.8 MPa. The Young's modulus of the MMMs increased to 1029.5 MPa when the MC-MX loading was raised to 1.0 wt%, with concomitant improvements in elongation strain and tensile strength. This suggested the presence of hydrogen-bond interactions between MC-MX and Pebax subsequent to the addition of MC-MX. The Young's modulus of MMMs decreased as the loading was further increased, due to the slight load displacement caused by MC-MX aggregation.

As shown in Fig. 3h and Fig. S8, the water contact angle of MMMs decreased with the increase of MC-MX loading. This is attributed to the enhanced hydrophilicity resulting from the hydrogen bonding interactions between the abundant -OH groups on MC-MX and water molecules.

DFT calculations were performed to unravel the atomic-level mechanism behind CO_2 affinity enhancement in MC-MX. As shown in Figs. 4a-d, the adsorption energy (E_{ads}) followed: MC-MX···CO_2 (−7.72 eV) > MC-MX···CH_4 (−2.30 eV) > MX···CO_2 (−1.12 eV) > MX···CH_4 (−0.21 eV). The enhanced difference in E_{ads} between CO_2 and CH_4 on MC-MX originated from hydrogen-bond interactions between CO_2 and hydroxyl–functionalized interfaces. The abundant -OH termination groups on MX surfaces enabled MX to act as CO_2-selective tollgates, preferentially enriching CO_2 at the filler-polymer interface due to strong dipole-quadrupole interactions. Concurrently, hydrogen-bond mediation between MC and CO_2 facilitated rapid transport along the ordered nanochannels within the MC network. This synergistic effect enabled the Pebax/MC-MX MMMs to simultaneously enhance both selectivity and permeability.

As illustrated in Fig. 5a, both the diffusion coefficients of CO_2 (D_{CO_2}) and CH_4 (D_{CH_4}) exhibited a progressive rise with increasing MC-MX loading. Notably, the enhancement in D_{CO_2} diffusion significantly surpassed that of D_{CH_4}. This was mainly due to the preferential diffusion pathway of CO_2 in the MC-MX structure. The interconnected network structure of MC-MX established preferen-

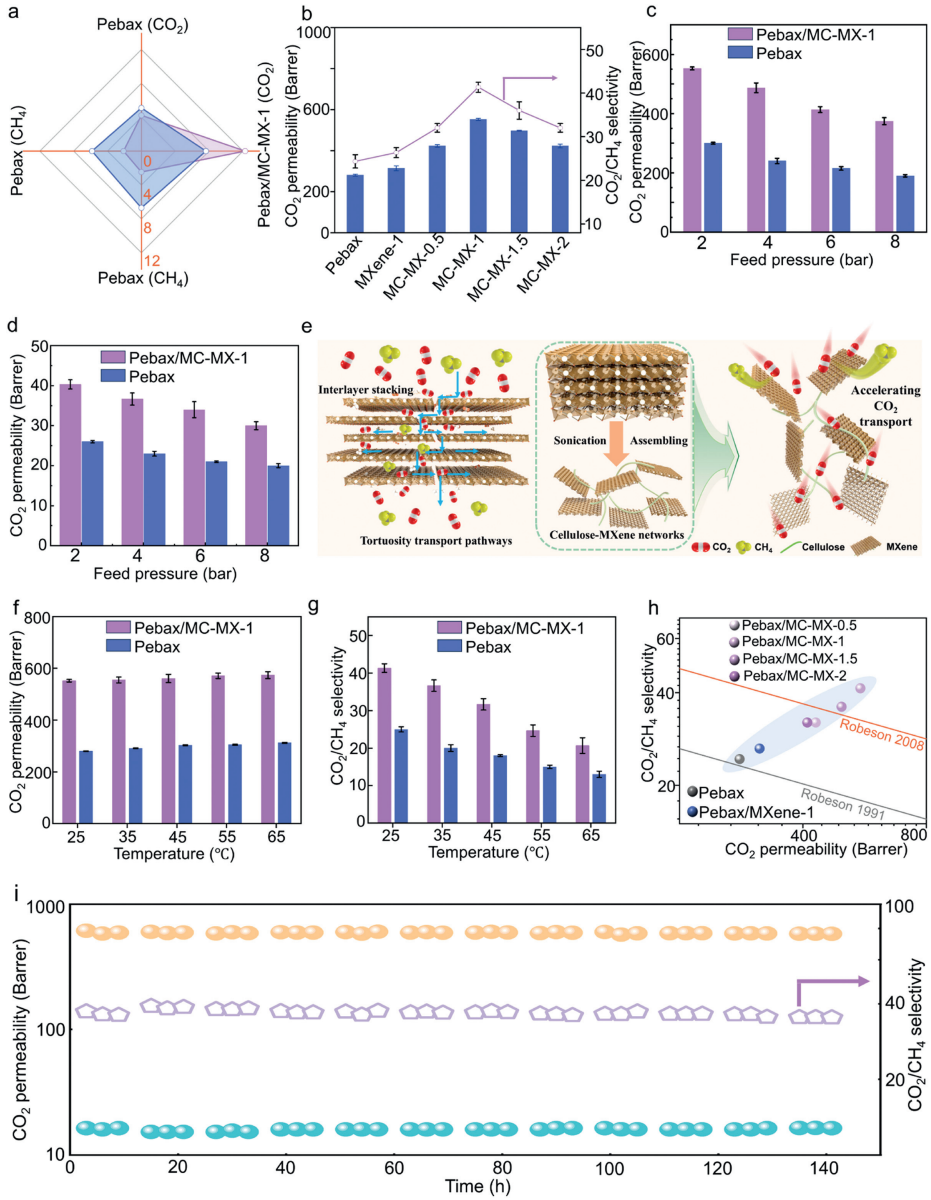


Fig. 5. (a) CO_2 and CH_4 diffusion and solubility coefficients. (b) Comparison of separation performances of the MMMs. (c) Permeability and (d) selectivity of membranes with different operating pressure. (e) The schematic illustration of transport. (f) Permeability and (g) selectivity of membranes with different operating temperature. (h) CO_2/CH_4 separation performance of MMMs vs. upper bounds. (i) Long-term operational stability for CO_2/CH_4 separation.

tially facilitate CO_2 transport pathways, thereby enhancing diffusion selectivity. The solubility coefficient and the solubility selectivity of CO_2/CH_4 in Pebax/MC-MX MMMs both increased compared with pure Pebax membranes. These findings suggested that the incorporation of MC-MX into Pebax membranes effectively improves CO_2/CH_4 mixtures separation performance.

As shown in Fig. 5b, the Pebax/MC-MX MMMs exhibited significant improvements in both CO_2 permeability and selectivity compared with the pure Pebax membrane. The Pebax/MC-MX-1 MMMs demonstrated a CO_2 permeability of 580.5 Barrer and a CO_2/CH_4 selectivity of 41.5 ($V_{CO_2}/V_{CH_4} = 20/80$). Compared to the pure Pebax membrane, there were 97 % and 70 % enhancements in permeability and selectivity, respectively. This excellent membrane performance was mainly attributed to the "tollgate-highway" system in the MC-MX, which improved the CO_2 separation performance of the MMMs. Firstly, the MC interwoven with MX suppressed interlayer stacking, forming continuous "highways" that facilitated CO_2 transport. Secondly, the hydroxyl groups on MX surfaces acted as hydrogen-bonding selective "tollgates", which preferentially interacted with CO_2.

As depicted in Figs. 5c and d, the CO_2 and CH_4 permeabilities and the CO_2/CH_4 selectivity of the MMMs were compared under different feed pressures (2–8 bar). The permeability and selectivity of pure Pebax membranes and Pebax/MC-MX-1wt% MMMs decreased as the operating pressure increased from 2 bar to 8 bar. According to Henry's law, where gas solubility (S) was inversely proportional to pressure (P), elevated pressure reduced the sorption capacity, thereby diminishing the separation performance. CO_2 exhibited higher condensability compared to CH_4, which enhanced the sensitivity of CO_2 solubility to pressure changes.

As shown in Figs. 5f and g, the CO_2 and CH_4 permeability of MMMs increased with the rise of operating temperature, while the CO_2/CH_4 selectivity decreased. This phenomenon primarily stems from elevated temperatures enhanced polymer chain mobility, which promotes the formation of transient free volume cavities. The lower activation energy barrier CH_4 preferentially occupies these cavities, thereby accelerating the permeation of CH_4 and reducing the selectivity of the MMMs. The enhancement in CH_4 permeability compared to CO_2 under elevated temperatures arose from CH_4 lower activation energy for diffusion, consequently reducing the CO_2/CH_4 separation selectivity by 50 %.

As illustrated in Figs. 5e and h, the incorporation of MC-MX networks significantly enhanced the CO_2/CH_4 separation performance of the fabricated MMMs. The Pebax/MC-MX-1wt% MMMs demonstrated the best separation performance, surpassing the 2008 Robeson upper bound. Furthermore, compared to the Pebax-based MMMs reported in the literature, the Pebax/MC-MX-1wt% MMMs exhibited higher permeability and selectivity (Table S7 in Supporting information). To verify the stability of the Pebax/MC-MX-1wt% MMMs, we perform a 140 h of long-term separation performance test (Fig. 5i). The results show that Pebax/MC-MX-1wt% MMMs had excellent long-term stability, and its permeability and selectivity did not decrease significantly.

This remarkable performance improvement could be attributed to the unique structure of the MC-interwoven MX network, which addresses the trade-off between permeability and selectivity in MMMs. The 1D MC-interwoven MX network eliminated interlayer stacking, creating continuous low-tortuosity pathways that function as CO_2 "highways", which significantly enhanced permeability. The MX surface -OH groups construct hydrogen-bonding "tollgates" that not only selectively interacted with CO_2 through specific recognition, thereby enhancing selectivity. This indicated that the introduction of tollgate-highway system was a promising strategy to construct advanced MMMs for gas separations. Compared with conventional separation methods (amine absorption and cryogenic distillation) and state-of-the-art MMMs (Table S7), the Pebax/MC-MX MMMs achieved a simultaneous breakthrough in CO_2 permeability and selectivity under room-temperature and low-pressure conditions. Notably, the MMM separation process offers low energy consumption without high-temperature regeneration or solvent emissions, demonstrating superior industrial scalability and environmental friendliness.

This work demonstrated that incorporating MC-MX networks into Pebax to prepare MMMs constructs a mimetic tollgate-highway system, which greatly improved CO_2/CH_4 separation performance. The MX nanosheets act as selective tollgates that preferentially interact with CO_2 though hydrogen bonding, thereby enhancing CO_2 selectivity and inhibiting CH_4 transport. Meanwhile, the interweaving MC effectively inhibited MX stacking while established continuous CO_2 transport highways, enabling accelerated CO_2 transport through low-resistance transport. The Pebax/MC-MX-1wt% MMM obtained a CO_2 permeability of 580.46 Barrer (97 %) and a CO_2/CH_4 selectivity of 41.48 (70 %), positioning it near the 2019 upper bound for MMMs. These outcomes demonstrate that efficient CO_2 separation can be achieved through structurally synergistic transport highways in MMMs, offering a novel strategy to advance membrane separation performance.

Declaration of competing interest

The authors declare that they have no known competing financial interests or personal relationships that could have appeared to influence the work reported in this paper.

CRediT authorship contribution statement

Yong Zhang: Writing – review & editing, Writing – original draft, Visualization, Conceptualization. **Jiangnan Yu:** Methodology, Data curation. **Chao Liang:** Visualization, Data curation. **Zhaomin Li:** Supervision, Funding acquisition. **Xueqin Li:** Writing – review & editing, Writing – original draft, Funding acquisition.

Acknowledgments

This work was supported by the Science and Technology Research Program for Key Fields of Province (No. 2023AB011), the Achievement Transformation and Technology·Promotion Program of Shihezi University (No. CGZH202304).

Supplementary materials

Supplementary material associated with this article can be found, in the online version, at doi:10.1016/j.cclet.2025.112065.

References

[1] S. Ganesan, R. Canevesi, C. Grande, Ind. Eng. Chem. Res. 63 (2024) 18497–18512.
[2] A. Abd, J. Kim, D. Jasim, M. Othman, Energy Convers. Manag. 321 (2024) 119090.
[3] H. Gong, Z. Chen, H. Yu, et al., Energy 157 (2018) 744–751.
[4] D. Turunawarasu, Y. Wong, J. Sunarso, et al., Ind. Eng. Chem. Res. 64 (2025) 1664–1679.
[5] R. Hou, J. Yu, J. Xie, et al., Sep. Purif. Technol. 360 (2025) 131077.
[6] T. Wang, K. Zhang, S. Du, et al., Chem. Eng. J. 477 (2023) 147280.
[7] Q. Qian, A. Wright, H. Lee, M. Dincă, Z. Smith, Chem. Mater. 33 (2021) 6825–6831.
[8] J. Wang, L. Li, J. Zhang, X. Li, J. Membr. Sci. 697 (2024) 122569.
[9] B. Wang, M. Sheng, J. Xu, et al., Small Methods 4 (2020) 1900749.
[10] F. Shi, J. Sun, J. Wang, et al., J. Membr. Sci. 620 (2021) 118850.
[11] G. Liu, L. Cheng, G. Chen, et al., Chem. Asian J. 15 (2020) 2364–2370.
[12] W. Guan, X. Yang, C. Dong, et al., J. Appl. Polym. Sci. 138 (2021) 49895.
[13] I. Ahmad, H. Jee, S.H. Song, et al., Mater. Today Sustain. 23 (2023) 100410.
[14] W. Fam, J. Mansouri, H. Li, J. Hou, V. Chen, ACS Appl. Mater. Interfaces 10 (2018) 7389–7400.
[15] X. Yao, D. Cui, C. Zhu, et al., ACS Mater. Lett. 6 (2024) 5112–5119.
[16] M. Liu, L. Zhang, J. Rostami, et al., ACS Nano 19 (2025) 13399–13413.

[17] Z. Hu, Y. Yang, X. Zhang, C. Xu, J. Yao, Sep. Purif. Technol. 326 (2023) 124704.
[18] G. Jia, Z. Wang, M. Gong, et al., Carbon Energy 5 (2023) e270.
[19] Y. Xu, Z. Zhang, Z. Cui, et al., Chem. Eng. J. 488 (2024) 151078.
[20] F. Liu, S. Wang, C. Zhao, B. Hu, Biochar 5 (2023) 31.
[21] H. Tian, J. Yan, A. Rajulu, A. Xiang, X. Luo, Int. J. Biol. Macromol. 96 (2017) 518–523.
[22] J. Shen, M. Zhang, G. Liu, K. Guan, W. Jin, AlChE J. 62 (2016) 2843–2852.
[23] S. Grabowski, W. Sokalski, J. Leszczynski, J. Phys. Chem. A 109 (2005) 4331–4341.
[24] R. Xu, Y. Kang, W. Zhang, B. Pan, X. Zhang, Nat. Commun. 14 (2023) 4907.
[25] Z. Wang, L. Ban, P. Meng, H. Li, Y. Zhao, Nanomaterials 9 (2019) 1137.
[26] K. Duan, J. Wang, Y. Zhang, J. Liu, J. Membr. Sci. 572 (2019) 588–595.
[27] Z. Qin, Y. Ma, W. Du, et al., Sep. Purif. Technol. 344 (2024) 126831.
[28] N. Liu, J. Cheng, L. Hu, et al., Chem. Eng. J. 427 (2022) 130845.
[29] S. Nilouyal, H. Karahan, A. Isfahani, et al., ACS Appl. Mater. Interfaces 14 (2022) 37595–37607.
[30] M. Kheirtalab, R. Abedini, M. Ghorbani, Process Saf. Environ. Prot. 144 (2020) 208–224.